The Astrophysical Journal, 914:10 (15pp), 2021 June 10 https://doi.org/10.3847/1538-4357/abfa23

On the Use of Field RR Lyrae as Galactic Probes. III. The α-element Abundances*

J. Crestani[1,2,3], V. F. Braga[2,4], M. Fabrizio[2,4], G. Bono[1,2], C. Sneden[5], G. Preston[6], I. Ferraro[2], G. Iannicola[2], M. Nonino[7], G. Fiorentino[2], F. Thévenin[8], B. Lemasle[9], Z. Prudil[9], A. Alves-Brito[3], G. Altavilla[2,4], B. Chaboyer[10], M. Dall'Ora[11], V. D'Orazi[12,13], C. Gilligan[10], E. K. Grebel[9], A. J. Koch-Hansen[9], H. Lala[9], M. Marengo[14], S. Marinoni[2,4], P. M. Marrese[2,4], C. Martínez-Vázquez[15], N. Matsunaga[16], M. Monelli[17], J. P. Mullen[14], J. Neeley[18], R. da Silva[2,4], P. B. Stetson[19], M. Salaris[20], J. Storm[21], E. Valenti[22,23], and M. Zoccali[24]

[1] Dipartimento di Fisica, Università di Roma Tor Vergata, via della Ricerca Scientifica 1, I-00133 Roma, Italy; juliana.crestani@uniroma1.it
[2] INAF—Osservatorio Astronomico di Roma, via Frascati 33, I-00078 Monte Porzio Catone, Italy
[3] Departamento de Astronomia, Universidade Federal do Rio Grande do Sul, Av. Bento Gonçalves 6500, Porto Alegre 91501-970, Brazil
[4] Space Science Data Center—ASI, via del Politecnico snc, I-00133 Roma, Italy
[5] Department of Astronomy and McDonald Observatory, The University of Texas, Austin, TX 78712, USA
[6] The Observatories of the Carnegie Institution for Science, 813 Santa Barbara St., Pasadena, CA 91101, USA
[7] INAF—Osservatorio Astronomico di Trieste, Via G. B. Tiepolo 11, I-34143 Trieste, Italy
[8] Université de Nice Sophia-antipolis, CNRS, Observatoire de la Côte d'Azur, Laboratoire Lagrange, BP 4229, F-06304 Nice, France
[9] Astronomisches Rechen-Institut, Zentrum für Astronomie der Universität Heidelberg, Mönchhofstr. 12-14, D-69120 Heidelberg, Germany
[10] Department of Physics and Astronomy, Dartmouth College, Hanover, NH 03784, USA
[11] INAF—Osservatorio Astronomico di Capodimonte, Salita Moiariello 16, I-80131 Napoli, Italy
[12] INAF—Osservatorio Astronomico di Padova, vicolo dell'Osservatorio 5, I-35122, Padova, Italy
[13] School of Physics and Astronomy, Monash University, Clayton, VIC 3800, Melbourne, Australia
[14] Department of Physics and Astronomy, Iowa State University, Ames, IA 50011, USA
[15] Cerro Tololo Inter-American Observatory, NSF's National Optical-Infrared Astronomy Research Laboratory, Casilla 603, La Serena, Chile
[16] Department of Astronomy, The University of Tokyo, 7-3-1 Hongo, Bunkyo-ku, Tokyo 113-0033, Japan
[17] Instituto de Astrofísica de Canarias, Calle Via Lactea s/n, E-38205 La Laguna, Tenerife, Spain
[18] Department of Physics, Florida Atlantic University, 777 Glades Rd, Boca Raton, FL 33431, USA
[19] Herzberg Astronomy and Astrophysics, National Research Council, 5071 West Saanich Road, Victoria, British Columbia V9E 2E7, Canada
[20] Astrophysics Research Institute, Liverpool John Moores University, IC2, Liverpool Science Park, 146 Brownlow Hill, Liverpool, L3 5RF, UK
[21] Leibniz-Institut für Astrophysik Potsdam (AIP), An der Sternwarte 16, D-14482 Potsdam, Germany
[22] European Southern Observatory, Karl-Schwarzschild-Str. 2, D-85748 Garching bei Munchen, Germany
[23] Excellence Cluster ORIGINS, Boltzmann–Straße 2, D-85748 Garching bei München, Germany
[24] Instituto de Astrofísica, Facultad de Física, Pontificia Universidad Católica de Chile, Av. Vicuña Mackenna 4860, Santiago, Chile
Received 2021 March 9; revised 2021 April 9; accepted 2021 April 16; published 2021 June 9

Abstract

We provide the largest and most homogeneous sample of α-element (Mg, Ca, Ti) and iron abundances for field RR Lyrae (RRLs; 162 variables) by using high-resolution spectra. The current measurements were complemented with similar abundances available in the literature for 46 field RRLs brought to our metallicity scale. We ended up with a sample of old ($t \geqslant 10$ Gyr), low-mass stellar tracers (208 RRLs: 169 fundamental, 38 first overtone, and 1 mixed mode) covering 3 dex in iron abundance ($-3.00 \leqslant$ [Fe/H] $\leqslant 0.24$). We found that field RRLs are ~0.3 dex more α poor than typical halo tracers in the metal-rich regime ([Fe/H] $\geqslant -1.2$), while in the metal-poor regime ([Fe/H] $\leqslant -2.2$) they seem to be on average ~0.1 dex more α enhanced. This is the first time that the depletion in α elements for solar iron abundances is detected on the basis of a large, homogeneous, and coeval sample of old stellar tracers. Interestingly, we also detected a close similarity in the [α/Fe] trend between α-poor, metal-rich RRLs and red giants (RGs) in the Sagittarius dwarf galaxy as well as between α-enhanced, metal-poor RRLs and RGs in ultrafaint dwarf galaxies. These results are supported by similar elemental abundances for 46 field horizontal branch stars. These stars share with RRLs the same evolutionary phase and the same progenitors. This evidence further supports the key role that old stellar tracers play in constraining the early chemical enrichment of the halo and, in particular, in investigating the impact that dwarf galaxies have had in the mass assembly of the Galaxy.

Unified Astronomy Thesaurus concepts: RR Lyrae variable stars (1410); Pulsating variable stars (1307); Milky Way stellar halo (1060); High resolution spectroscopy (2096); Spectroscopy (1558)

Supporting material: machine-readable tables

1. Introduction

The chemical abundances of stellar atmospheres preserve the signature of the molecular clouds that formed them. While some of their elements can be altered during stellar evolution, such as the LiCNO group and (rarely) some neutron-capture elements, stellar atmospheres remain the ideal subjects of Galactic archeology. Different chemical species are formed by processes with their own mass and timescales and, coupled

* Based on observations obtained with the du Pont telescope at Las Campanas Observatory, operated by Carnegie Institution for Science. Based in part on data collected at Subaru Telescope, which is operated by the National Astronomical Observatory of Japan. Based partly on data obtained with the STELLA robotic telescopes in Tenerife, an AIP facility jointly operated by AIP and IAC. Some of the observations reported in this paper were obtained with the Southern African Large Telescope (SALT). Based on observations made with the Italian Telescopio Nazionale Galileo (TNG) operated on the island of La Palma by the Fundación Galileo Galilei of the INAF (Istituto Nazionale di Astrofisica) at the Spanish Observatorio del Roque de los Muchachos of the Instituto de Astrofisica de Canarias. Based on observations collected at the European Organisation for Astronomical Research in the Southern Hemisphere.

with the age of the stellar tracers of interest, reveal the chemical enrichment history of different components of the Galaxy.

The even-Z light elements that are multiples of He nuclei are called α elements. In the past, it was believed that they were created by the successive capture of He nuclei. However, it is now understood that, while several elements are commonly grouped under the banner of α elements, not all of them are created equally nor are all of them equally easy to measure (Woosley & Weaver 1995; McWilliam 2016; Curtis et al. 2019). In particular the noble gases Ne and Ar cannot be detected, and S is rarely measured in optical spectra (Gratton et al. 2004). A similar limitation applies to O; indeed, O abundances are typically based either on two weak O I forbidden lines (6300, 6363 Å) or on O I triplet lines (7774, 9263 Å) that are affected by temperature uncertainties and by non-LTE effects (McWilliam 1997). Like oxygen, the much easier to measure Mg is created in the hydrostatic evolution of massive stars and released on supernovae type II (SNe II) events.

It is affected by the reaction mechanisms known as the "p-process" (Wallerstein et al. 1997), i.e., the production of proton-rich nuclei by a proton-capture mechanism. The other three species with easily detectable lines are Si, Ca, and Ti. Of these, the first two are likely mainly produced during Type II supernova (SN II)events, being thus considered "explosive" α elements. The third, Ti, has a vast number of absorption lines that can be detected on a broad wavelength and metallicity range. It is sometimes considered as an iron-peak element (Timmes et al. 1995) with possibly multiple formation channels. Indeed, its dominant isotope is actually $^{48}_{22}$Ti, which is not a multiple of an α particle. Yet the trend of titanium with metallicity follows quite well those of other α elements and suggests that, regardless of the precise formation channels, these chemical species are formed at similar rates in similar astrophysical sites.

Stellar evolution models point to SNe Ia as the result of thermonuclear explosions triggered by the binary interaction between an accreting white dwarf and its companion. The presence of a white dwarf implies a timescale of the order of billions of years. The yields of such explosions carry mostly iron, and so an environment enriched mostly by SNe Ia would have a decreasing [α/Fe] ratio as iron abundance increases. Indeed, in the [α/Fe] versus [Fe/H] plane, this decrease is commonly called the "knee," and is associated with the metallicity at which the SNe Ia began to dominate the enrichment of the interstellar medium (e.g., Matteucci & Brocato 1990).

The main producers of α elements, however, are the SNe II. They are the result of the core collapse of massive stars ($\gtrsim$8 $M_{\odot}$), with a timescale of the order of 1 to 10 million years. They enrich the interstellar medium with both iron and α elements, with the yields of the latter increasing as the mass of the SN II progenitor increases (Kobayashi et al. 2006). This means that the slope of the [α/Fe] abundance ratio and, in particular, its spread at fixed iron content can provide firm constraints on the variation of the initial mass function (IMF) as a function of both time and environment (McWilliam et al. 2013; Hendricks et al. 2014a; Lemasle et al. 2014; Reichert et al. 2020).

Thus, the fine structure of the [α/Fe] abundance ratio as a function of iron abundance has been in the intersection of several theoretical and empirical investigations (Matteucci & Greggio 1986). For over 40 years, α elements have been known to be enhanced in primarily old and metal-poor populations such as field halo stars and globular clusters (GCs) (Wallerstein et al. 1963; Sneden et al. 1979; Cohen 1981; Pilachowski et al. 1983; McWilliam 1997; Venn et al. 2004; Pritzl et al. 2005; Carretta et al. 2009a). The current evidence is suggesting a steady decrease in the [α/Fe] abundance ratio for iron abundances more metal rich than [Fe/H] ≈ -0.7. However, the number of truly old, metal-rich stellar tracers is quite limited (see Figures 10 and 11 in Gonzalez et al. 2011). Indeed, it is not clear yet whether old stellar tracers display the same slope in the [α/Fe] versus [Fe/H] plane as intermediate and young disk stellar populations in approaching solar iron abundance.

Two major concerns are involved in the selection of the stellar sample to be employed in the investigation of the chemical enrichment history of the halo. First, although the [α/Fe] abundance ratio is a solid diagnostic, stars covering a broad range in iron abundances with homogeneous and accurate estimates are necessary. Second, any discussion of chemical enrichment history must necessarily take into account the age of the stellar tracers that are being employed. Individual age estimates for field stars require very precise reddening and distance measurements, and therefore, samples of field stars suffer various degrees of contamination. For field RGs, this limitation becomes even more severe because they originate from progenitors that cover a broad range in mass. The natural targets for age-related experiments are GCs because they have accurate individual age estimates provided by isochrone fitting (e.g., Salaris & Weiss 1998; VandenBerg et al. 2013). However, the current spectroscopic investigations that are focused on GCs include only a few metal-rich systems (Pritzl et al. 2005; Carretta et al. 2009a, 2009b, 2010a; Gonzalez et al. 2011).

These two concerns can be addressed at once with the use of field RR Lyrae (RRL) variable stars. RRLs are solid tracers of old stellar populations, well known to be evolved low-mass stars with ages necessarily greater than 10 Gyr (Walker et al. 2019; Savino et al. 2020). They can be identified by the shape, period, and amplitude of their photometric light curves, all of which are reddening and distance independent. Their classification, coupled with spectroscopic atmospheric parameters, provides a strongly univocal identification and makes any sample contamination extremely unlikely. The RRLs also are known to cover a broad range in metallicity (Wallerstein et al. 2012; Chadid et al. 2017; Sneden et al. 2017; Crestani et al. 2021) and far outnumber GCs. Indeed, while only roughly 180 GCs have been identified in the Galaxy (Harris 1996, 2010), the number of field RRLs thanks to long-term photometric surveys and to Gaia is at least a thousand times larger.[25] This means that the RRLs can trace the variation of chemical abundances across the Galactic spheroid with very high spatial resolution. The variation in the stellar mass of RRLs is at most of the order of 30%–40%, i.e., from $\approx$0.60 to $\approx$0.85 $M_{\odot}$; therefore, they are only minimally affected by the shape of the IMF. Moreover, the RRLs are also minimally affected by the time dependence, because they formed on a time interval of the order of 2 Gyr.

In the current work, we aim to investigate the impact that stellar age has on the [α/Fe] versus [Fe/H] plane using high-

[25] The current number is still severely underestimated because we lack a complete census of RRLs in the inner bulge and beyond.

resolution, high signal-to-noise ratio (S/N) spectra of 162 field RRLs. Among them, 138 are fundamental mode pulsators (RRab), 23 first overtone pulsators (RRc), and 1 mixed-mode pulsator (RRd). This data set is described in Section 2. The current homogeneous measurements of α-element and iron abundances were complemented with similar measurements for field RRLs and HB stars available in the literature and brought to our scale, as described in Section 3. In Section 4 we address how the atmospheric parameters and chemical abundances were computed. Results are shown and discussed in Section 5. In Section 6, we summarize this investigation and briefly outline future perspectives.

2. Spectroscopic Data Set

We collected a sample of 407 high-resolution (HR) spectra for 162 field RRLs (138 RRab, 23 RRc, 1 RRd). In order to obtain a high-enough S/N ($\gtrapprox$50 per pixel) for chemical abundance analysis, we stacked low-S/N spectra of the same star acquired at the same phase and with the same spectrograph, as described in more detail further below. This process resulted in 243 spectra that were analyzed individually. Among them, 51 were acquired with the echelle spectrograph at du Pont (Las Campanas Observatory), 74 with UVES (Dekker et al. 2000), and 16 with X-shooter (Vernet et al. 2011) at VLT (ESO, Cerro Paranal Observatory); 18 with HARPS (Mayor et al. 2003) at the 3.6 m telescope and 2 with FEROS (Kaufer et al. 1999) at the 2.2 m MPG telescope (ESO, La Silla Observatory); 5 with HARPS-N (Cosentino et al. 2012) at the Telescopio Nazionale Galileo (Roque de Los Muchachos Observatory); 47 with HRS (Crause et al. 2014) at SALT (South African Astronomical Observatory); 28 with the HDS (Noguchi et al. 2002) at Subaru (National Astronomical Observatory of Japan); and 2 with the echelle spectrograph (Weber et al. 2012) at STELLA (Izaña Observatory).

Representative spectra for each of these spectrographs are shown in Figure 1. Their typical wavelength ranges, resolutions, and S/Ns are listed in Table 1.

Continuum normalization and Doppler-shift corrections were made using the National Optical Astronomy Observatory libraries for IRAF[26] (Image Reduction and Analysis Facility; Tody 1993). Further information about the sample selection and radial velocity studies for the spectra analyzed in this work can be found in Fabrizio et al. (2019), Bono et al. (2020), and Crestani et al. (2021).

The stacking of spectra was performed after these steps. We made an initial selection based on phase, followed by a visual inspection. This ensured that all the spectra to be stacked displayed similar line depths and introduced no artifacts in the final stacked spectrum. Of the 243 final spectra that we analyzed, 178 were collected with high S/N and did not require stacking, 26 were the result of the stacking of two spectra, and 39 of three to seven spectra.

3. Spectroscopic Samples

The 162 RRLs described above form the This Work (TW-RRL) sample. Previous high-resolution metallicity measurements are available in the literature for 47 of these stars. They were used to transform iron and α-element abundances into a homogeneous abundance scale. This supplied us with 69 measurements for 46 stars made by nine previous works. Note that the measurements taken from For & Sneden (2010), For et al. (2011), Chadid et al. (2017), and Sneden et al. (2017) are natively in our scale and require no shifts. Indeed, a comparison between 23 RRLs measured both in those works

[26] The legacy code is now maintained by the community on GitHub at https://iraf-community.github.io/.

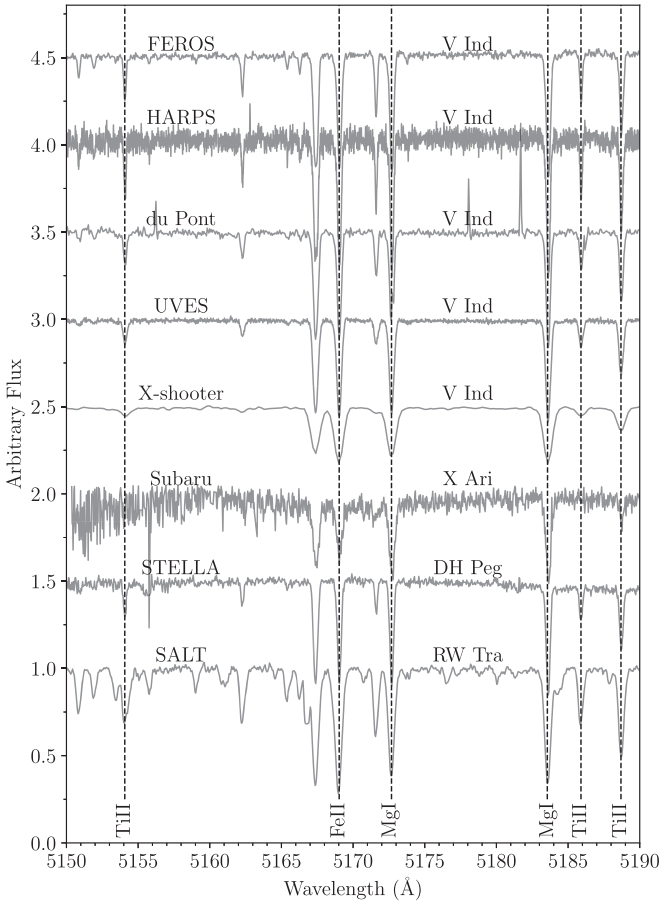

Figure 1. Representative high-resolution spectra for all spectrographs used in this work. The top five spectra are of V Ind ([Fe/H] = −1.63 ± 0.03, RRab) at the same pulsation phase. They are followed by random-phase spectra for X Ari ([Fe/H] = −2.59 ± 0.05, RRab), DH Peg ([Fe/H] = −1.37 ± 0.05, RRc), and RW Tra ([Fe/H] = 0.13 ± 0.06, RRab). The dashed lines indicate the iron and α-element absorption lines in this wavelength region.

Table 1
Typical Characteristics of Each Instrument Used in This Work

Spectrograph	Telescope	Wavelength Range (Å)	Resolution	S/N
echelle	du Pont	3700–9100	27,000	70
UVES	VLT	3000–6800	35,000–107,000	76
X-shooter	VLT	3000–10200	18,400	86
HARPS	3.6 m	3700–6900	80,000–115,000	45
FEROS	2.2 m MPG	3500–9200	48,000	53
HARPS-N	TNG	3900–6900	115,000	65
HRS	SALT	3900–8800	40,000	61
HDS	Subaru	5060–7840	60,000	95
echelle	STELLA	3860–8820	55,000	74

Note. The wavelength ranges and resolutions are approximate. Different instrumental configurations result in different values, including wavelength coverage gaps. The archival data for UVES displayed a significant variety of configurations. Only the most representative values are shown.

Table 2
Basic Information of the Entire RRL Sample

Gaia ID (DR2)	Star	R.A.$_{ICRS(2015.15)}$ (deg)	Decl.$_{ICRS(2015.15)}$ (deg)	*V*mag (mag)	*V*amp (mag)	*P* (day)	Class	Sample
4224859720193721856	AA Aql	309.5628	−2.8903	11.831	1.275	0.3618	RRab	TW-RRL
2608819623000543744	AA Aqr	339.0161	−10.0153	12.923	1.087	0.6089	RRab	TW-RRL
3111925220109675136	AA CMi	109.3299	1.7278	11.558	0.965	0.4763	RRab	TW-RRL
1234729400256865664	AE Boo	221.8968	16.8453	10.651	0.423	0.3149	RRc	TW-RRL
2150632997196029824	AE Dra	276.7780	55.4925	12.474	0.799	0.6027	RRab	Lit-RRL

Note. Identification, coordinates, average visual magnitude (*V*mag), visual amplitude (*V*amp), period (*P*), classification, and sample of the RRL stars.

(This table is available in its entirety in machine-readable form.)

Table 3
RRL Abundances Adopted from the Literature

Gaia ID (DR2)	[Fe/H]$_o$	[Mg/Fe]$_o$	[Ca/Fe]$_o$	[Ti/Fe]$_o$	[Fe/H]	[Mg/Fe]	[Ca/Fe]	[Ti/Fe]	Reference
15489408711727488	−2.480	0.47	0.45	0.43	−2.67	0.60	0.43	0.37	C95
15489408711727488	−2.470		0.29		−2.47		0.39		L96
15489408711727488	−2.190	0.47	0.29	0.80	−2.41	0.35	0.31	0.91	P15
2341083636832476l6	−0.280		0.14		−0.28		0.08		F96
2341083636832476l6	−0.230		−0.11		−0.23		−0.00		L96

Note. Identification, iron and α-element abundances in both their original (subscript *o*) scale and in our scale for the Lit-RRL sample. Note that the values adopted from For & Sneden (2010), For et al. (2011), Chadid et al. (2017), and Sneden et al. (2017) require no shifts to be in our metallicity and α-element abundance scale and therefore are not included in this table. See text for details. References and number of stars in common with the TW-RRL sample are C95, eight: Clementini et al. (1995); F96, four: Fernley & Barnes (1996), G14, two: Govea et al. (2014); L96, eight: Lambert et al. (1996); P15, eight: Pancino et al. (2015).

(This table is available in its entirety in machine-readable form.)

and in the present work resulted in absolute differences smaller than 0.10 dex for all abundances. Note that the investigation from For & Sneden (2010) was focused on nonvariable HB stars for which we did not perform a reanalysis, but they used the same line list, instrument, and methodology as For et al. (2011). Once all abundances of interest were brought to our scale, multiple measurements for the same star were averaged. This allowed us to form the Literature RRL (Lit-RRL) sample, with 46 stars. We will refer to the TW-RRL and Lit-RRL samples together as the RRL sample. Its basic characteristics are shown in Table 2. The individual measurements for the literature stars both in their native scale and in our scale are shown in Table 3, alongside their references.

For & Sneden (2010) investigated the chemical abundances of metal-poor field red HB stars, in our same metallicity and α-element scale. We found that two of their stars were later classified as RRL. One of them is already in the TW-Lit sample, and the other was added to the Lit-RRL sample. We adopted the data for the remaining HB stars as the Lit-HB sample, with 46 stars. The complete sample of RRL and HB stars in this work will be referred to as the RRL+HB sample.

4. Chemical Abundance Measurements

We have applied the same iron line list and LTE line analysis described in Crestani et al. (2021). In brief, equivalent widths were measured manually with the splot IRAF. We only considered lines with equivalent widths between 15 and 150 mÅ in order to avoid spurious measurements and saturated lines. We derived the effective temperature ($T_{\rm eff}$), surface gravity (log(g)), microturbulent velocity (ξ_t), and metallicity ([Fe/H]) for each atmosphere using the equivalent widths of the neutral and single-ionized iron lines. For this, we followed the method of iteratively changing the atmospheric parameters in order to achieve excitation equilibrium of Fe I lines ($T_{\rm eff}$), ionization equilibrium between Fe I and Fe II lines (log(g)), and no trend between the abundance of each individual Fe I line against its respective reduced equivalent width (ξ_t). This process was done using the 2019 release of MOOG[27] (Sneden 1973), the MOOG wrapper PYMOOGI[28] developed by M. Adamow, and an interpolated grid of α-enhanced ([α/Fe] = 0.4 dex) ATLAS9 model atmospheres (Castelli & Kurucz 2003). The adopted atmospheric values for each individual measurement are shown in Table 4.

Once the final model atmosphere was constrained, the abundances of the α elements were computed from the equivalent widths of their lines. The line list is shown in Table 5, alongside the reference for their excitation potential (EP) and oscillator strength (log(gf)). As with iron, only lines with equivalent widths between 15 and 150 mÅ were considered. Solar abundance values were adopted from Asplund et al. (2009). In the case where more than one line was available for a given chemical species, the median[29] value was adopted.

A single RRL can undergo changes as large as 1000 K in effective temperature and 1 dex in log(g) (For et al. 2011). Thus, the robustness of a given method of abundance determination can be assessed by its capacity to recover coherent values across the pulsation phase. Similarly, the difference between repeated measurements is a reliable

[27] The code and documentation can be found at https://www.as.utexas.edu/~chris/moog.html.

[28] The code and documentation can be found at https://github.com/madamow/pymoogi.

[29] In this work, we employ the μ and σ characters to denote, respectively, the median and the median absolute deviation.

Table 4
Atmospheric Parameters Derived in This Work for Each Individual Measurement

Gaia ID (DR2)	Spectrograph	$T_{\rm eff}$ (K)	log(g) (dex)	$\xi_{\rm t}$ (km s^{-1})	[Fe I/H] (dex)	$N_{\rm Fe\ I}$	[Fe II/H] (dex)	$N_{\rm Fe\ II}$	$N_{\rm stack}$
4224859720193721856	SALT	6610 ± 130	2.70 ± 0.12	2.52 ± 0.08	−0.34 ± 0.24	206	−0.34 ± 0.22	39	1
4224859720193721856	Subaru	6470 ± 110	2.62 ± 0.10	2.42 ± 0.08	−0.49 ± 0.17	137	−0.49 ± 0.16	22	1
2608819623000543744	UVES	5840 ± 160	1.52 ± 0.06	3.51 ± 0.25	−2.31 ± 0.10	37	−2.31 ± 0.12	13	1
3111925220109675136	SALT	7090 ± 180	3.01 ± 0.15	3.04 ± 0.16	0.24 ± 0.24	146	0.24 ± 0.21	19	1
1234729400256865664	HARPS	6630 ± 150	2.04 ± 0.08	2.79 ± 0.09	−1.62 ± 0.14	64	−1.62 ± 0.10	25	2

Note. Atmospheric parameters for each individual measurement of the TW-RRL sample. The columns $N_{\rm Fe\ I}$ and $N_{\rm Fe\ II}$ contain the number of adopted Fe I and Fe II lines, respectively. Column $N_{\rm stack}$ shows the number of individual exposures that are stacked in order to obtain the measurement. See text for details.

(This table is available in its entirety in machine-readable form.)

Table 5
List of α-element Transitions Adopted in This Work

Wavelength (Å)	Species	EP (eV)	log(gf) (dex)	Reference
3829.36	12.0	2.709	−0.227	NIST
4571.10	12.0	0.000	−5.620	NIST
4702.99	12.0	4.346	−0.440	NIST
5172.68	12.0	2.712	−0.393	NIST
5183.60	12.0	2.717	−0.167	NIST

Note. References—NIST: https://www.nist.gov/, LAW2013: Lawler et al. (2013), WOO2013: Wood et al. (2013).

(This table is available in its entirety in machine-readable form.)

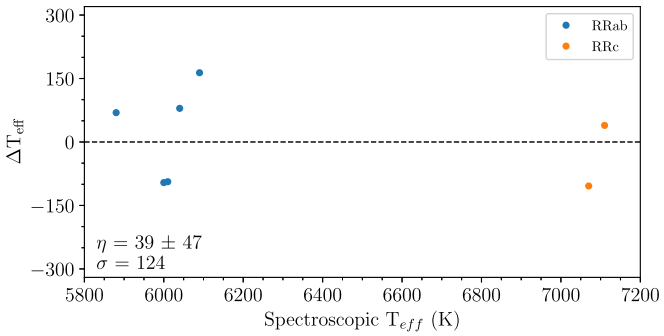

Figure 2. Difference between the photometric and spectroscopic effective temperatures $\Delta T_{\rm eff}$ for seven measurements of three RRLs. The median (η) and median absolute deviation (σ) of the difference are shown on the lower left. See text for details.

determination of the uncertainty of the measurements. With this in mind, we computed the uncertainties for iron and individual α elements by taking the median absolute deviation between multiple measurements for the same star both in the TW-RRL and Lit-RRL samples. For the TW-RRL sample, this allowed us to determine the typical uncertainty of each chemical species in each spectrograph, which we adopted for the stars with a single measurement. For stars with a single measurement in the Lit-RRL sample, we adopted a fixed uncertainty of 0.10 dex for iron and 0.15 for each α element. We averaged the abundances of Ti I and Ti II in order to derive a total [Ti/Fe] ratio. The [Ti I/Fe] and [Ti II/Fe] are on average shifted by 0.05 dex in our data. Any disagreements between Ti I and Ti II abundances are reflected in the uncertainties for each star.

To compute the total [α/H] abundance, we took the median of [Mg/H], [Ca/H], [Ti I/H], and [Ti II/H] according to their availability and weighted by their uncertainties. The median absolute deviation between the different α elements was adopted as the uncertainty in the total [α/H] abundance. Finally, we subtracted the iron abundance from [α/H] for each individual star to arrive at the final [α/Fe] value.

4.1. Verification of the T_{eff} Scale

The atmospheric parameter that most strongly affects the determination of chemical abundances is the effective temperature. As described above, it is essential that the methodology employed for chemical abundance analysis be capable of recovering coherent abundances across the pulsation cycle, i.e., at different values of $T_{\rm eff}$. It is already known that spectroscopic studies of RRL in both low and high resolution can achieve excellent precision at random phases (e.g., For et al. 2011; Crestani et al. 2021).

In order to have a sanity check independent of spectroscopy, we applied the photometric $T_{\rm eff}$ calibration of Alonso et al. (1999, 2001) to a subsample of RRL with V- and K-band photometry. The $V-K$ color was chosen because it is the least affected by uncertainties in the temperature and provides very stable results (Cacciari et al. 2000; Bono 2003). Photometric $T_{\rm eff}$ relations have a limited applicability to the RRLs because these stars cover a wide range of metallicities and moderately high temperatures (see, e.g., Table 1 in Alonso et al. 1999). As the RRL are variable stars with continuously changing colors, the application of these calibrations requires either simultaneous or well-sampled light curves in both optical and near-infrared bands. Moreover, the phasing itself requires very good determinations of both period and reference epoch. An added difficulty is that, in order to adopt photometric temperatures in a chemical abundance analysis, both photometric and spectroscopic data must be acquired for the same phase. Unfortunately, obtaining all the necessary data for these paired observations is not trivial.

Fortunately enough, we found well-sampled $V-K$ color curves for three variables with a total of seven spectra in the TW-RRL sample: DH Peg (RRc, [Fe/H] = −1.36, two spectra), VY Ser (RRab, [Fe/H] = −1.96, three spectra), and W Tuc (RRab, [Fe/H] = −1.90, two spectra). The photometry was taken from Jones et al. (1988), Barnes et al. (1988), Liu & Janes (1989), Clementini et al. (1990), Fernley et al. (1990), and Cacciari et al. (1992). We found a very good agreement between photometric and spectroscopic estimates, with residuals displaying a median $\eta = 39 \pm 47$ K and median absolute deviation $\sigma = 124$ K (Figure 2).

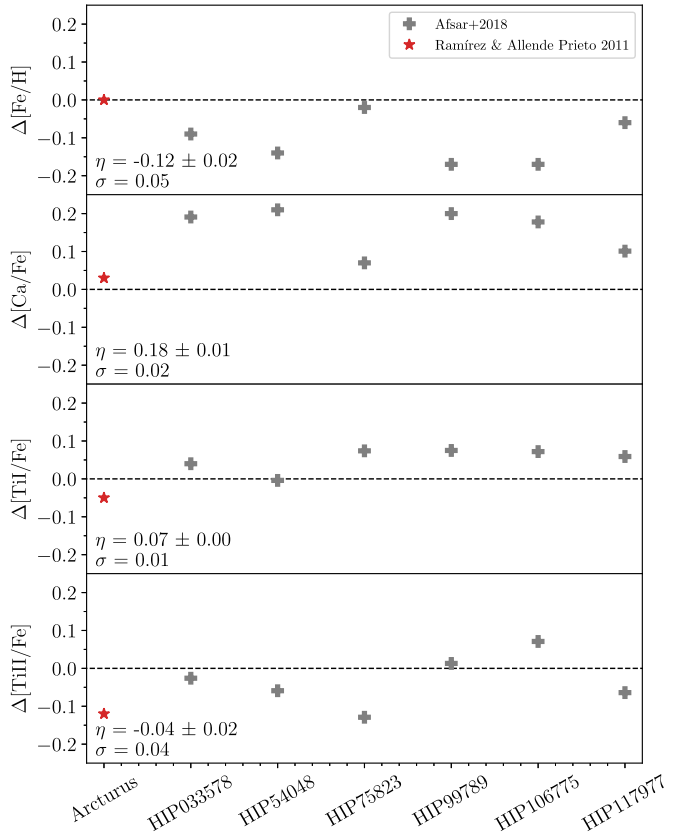

Figure 3. Difference between the iron and α-element abundances derived in this work and those of Afsar et al. (2018) for a sample of six HB stars, shown as gray crosses. The median (η) and median absolute deviation (σ) of the difference are shown in each panel. A red star shows the same difference for Arcturus (Ramírez & Allende Prieto 2011).

4.2. Validation of the α-element Abundance Scale

The validation of our metallicity scale was performed in Crestani et al. (2021). For the validation of our α-element abundance scale, we performed three tests. First, we analyzed one high-S/N (≈350), high-dispersion ($R = 115{,}000$) spectrum for Arcturus collected with HARPS. We found the atmospheric parameters $T_{\rm eff} = 4350 \pm 60$ K, $\log(g) = 1.65 \pm 0.07$, $\xi_{\rm t} = 1.75 \pm 0.04$ kms^{-1}, and chemical abundances[30] [Fe I/H] $= -0.52 \pm 0.06$, [Fe II/H] $= -0.52 \pm 0.20$, [Ca/Fe] $= 0.08 \pm 0.14$, [Ti I/Fe] $= 0.32 \pm 0.20$, and [Ti II/Fe] $= 0.33 \pm 0.09$ dex. These results are in excellent agreement with Ramírez & Allende Prieto (2011). Indeed, the difference in the abundances is 0.00, 0.03, −0.05, and −0.12 for Fe, Ca, Ti I, and Ti II, respectively. Unfortunately, the Mg lines in our line list, optimized for hotter stars, were all saturated in the much colder atmosphere of Arcturus. Second, we performed the same analysis on six red HB stars investigated by Afsar et al. (2018). These stars are only slightly colder than the RRL. The results are shown in Figure 3, and once again, they agree quite well with literature estimates. Third, we made a comparison using directly the equivalent widths of iron and α elements for several pairs of stars at similar effective temperature. The analysis of these paired spectra is discussed in Appendix A.

[30] The listed uncertainties in the chemical abundances for Arcturus are only due to the uncertainties in $T_{\rm eff}$, $\log(g)$, and $\xi_{\rm t}$.

We verified that NLTE corrections do not change the conclusions of our investigation (Section 5). As most works in the literature do not make use of such corrections, we opted to not apply them in order to better compare our results to previous ones. Ca, Ti I, and Ti II display a few lines that appear in all metallicity regimes and allowed us to verify that the averages for each species are not affected by systematics between lines. For Mg, no individual line is measurable in the entire metallicity range, but different lines have superposed metallicity regimes, e.g., one line appears in stars from metal poor to intermediate, and another from metal intermediate to rich. These considered together exhibit a coherent trend with each other and with both Ca and Ti. We refer the reader to Appendix B for a detailed discussion of both the NLTE corrections and the behavior of individual lines.

5. Results and Discussion

5.1. The Individual Species

The final metallicity, individual α-element abundance, and total [α/Fe] abundance for each RRL and HB star are shown in Table 6. The coverage in pulsational amplitude and period of the full RRL sample is shown in the top panels of Figure 4. The bottom panel of the same figure shows the same sample, but color-coded according to metallicity (see the color bar on the right side).

Fundamental RRLs located in the high-amplitude, short-period ($P \lesssim 0.48$ days) region, i.e., the so-called HASP region, are confirmed to be more metal rich than −1.5 dex, as expected from low-resolution spectra and GC metallicities (see Fiorentino et al. 2015, 2017). The precision of the current iron abundances strengthens the evidence that the HASPs trace quite well the transition from fundamental to first overtone RRLs. The RRc seems to show a similar trend: their metal-rich tail is traced by short-period variables ($P \leqslant 0.27$ days), although their luminosity amplitudes have typical RRc values. However, the number of metal-rich RRc variables is still too limited to constrain their pulsation properties close to the blue (hot) edge of the RRL instability strip.

The [X/Fe] versus [Fe/H] plane for each α element of interest is shown in Figure 5 with both the RRL and the Lit-HB samples. Several interesting features are visible and worth being discussed in detail.

(i) *Similar trends for RRL and HB stars*—The targets plotted in Figure 5 come from the same evolutionary path. The current empirical and theoretical evidence indicates that blue HB, RRL, and red HB stars are old ($t \geqslant 10$ Gyr), low-mass ($M \approx 0.50$–$0.95\,M_{\odot}$) stars in their central helium-burning phase. They have very similar helium core masses ($\sim 0.50\,M_{\odot}$), and their key difference is in the envelope mass. A steady decrease in the envelope mass causes a systematic increase in the effective temperature moving the stellar structure from the red HB to the blue HB, passing through the RRL instability strip. There is evidence that some RRLs are the aftermath of close binary evolution and could be younger objects (Pietrzyński et al. 2012; Karczmarek et al. 2017). However, the fraction of RRLs in binary systems is of the order of a few percent (Hajdu et al. 2015; Kervella et al. 2019; Prudil et al. 2019), and the figure for systems with mass transfer is likely to be even more modest. In all our spectroscopic investigations with the present sample, we found no evidence of binarity.

Table 6
Abundances for the RRL and Lit-HB Samples

Gaia ID (DR2)	[Fe/H] (dex)	[Mg/Fe] (dex)	[Ca/Fe] (dex)	[Ti/Fe] (dex)	[α/Fe] (dex)	Sample	Source
1548940871172748 8	-2.53 ± 0.08	0.49 ± 0.20	0.37 ± 0.20	0.42 0.20	0.37 ± 0.08	Lit-RRL	
5384844882991577 6	-1.40 ± 0.03	0.56 ± 0.14	0.28 ± 0.14	0.20 0.14	0.25 ± 0.05	Lit-HB	F10
7784937461710617 6	-1.77 ± 0.01	0.14 ± 0.03	0.10 ± 0.03	0.14 0.08	0.12 ± 0.01	TW-RRL	
8055692629554252 8	-1.87 ± 0.08	0.58 ± 0.12	0.34 ± 0.11	0.34 0.09	0.43 ± 0.09	TW-RRL	
2341083636832476 16	-0.25 ± 0.02		0.04 ± 0.20		0.04 ± 0.06	Lit-RRL	

Note. Final abundances for the RRL and Lit-HB samples in our metallicity and α-element abundance scale. The stars with Fe, Mg, Ca, and Ti abundances adopted directly (i.e., without averaging with values from multiple sources and without the application of any scale shifts) from either For & Sneden (2010, F10), For et al. (2011, F11), Chadid et al. (2017, C17), or Sneden et al. (2017, S17) have their source indicated in the last column.

(This table is available in its entirety in machine-readable form.)

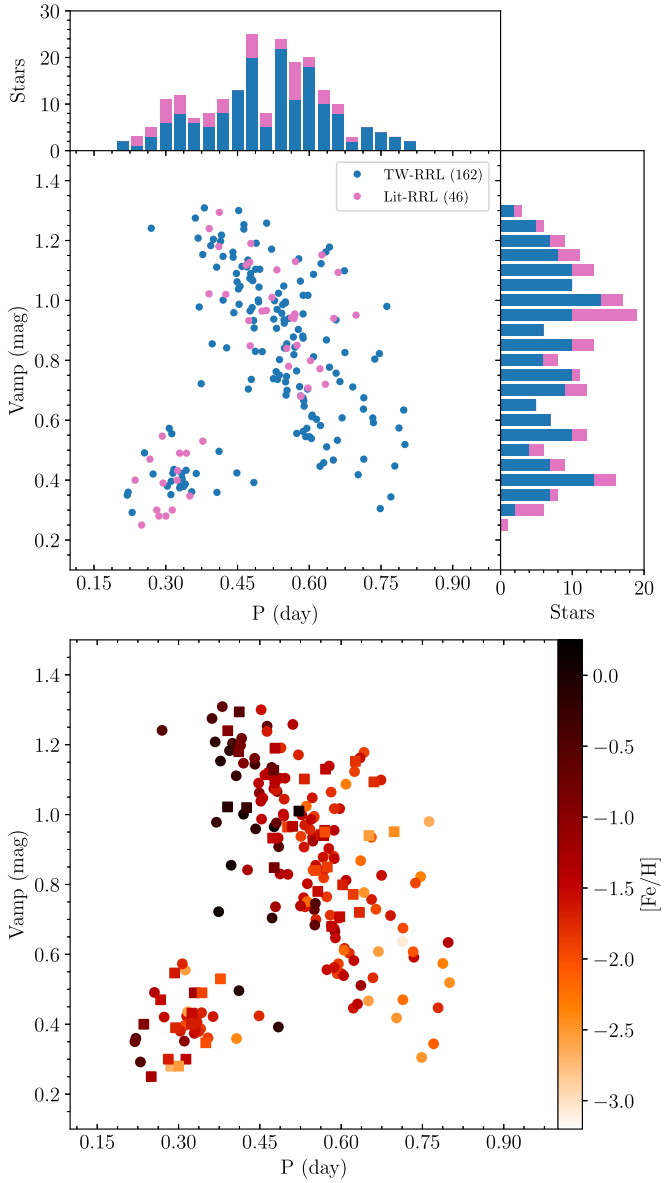

Figure 4. Top: Bailey diagram for the TW-RRL sample (blue) and the Lit-RRL sample (pink). The top and left histograms show the distribution of periods and *V*-band amplitudes, respectively. Bottom: Bailey diagram colored by metallicity according to the color bar on the right. The TW-RRL and the Lit-RRL stars are marked with circles and squares, respectively.

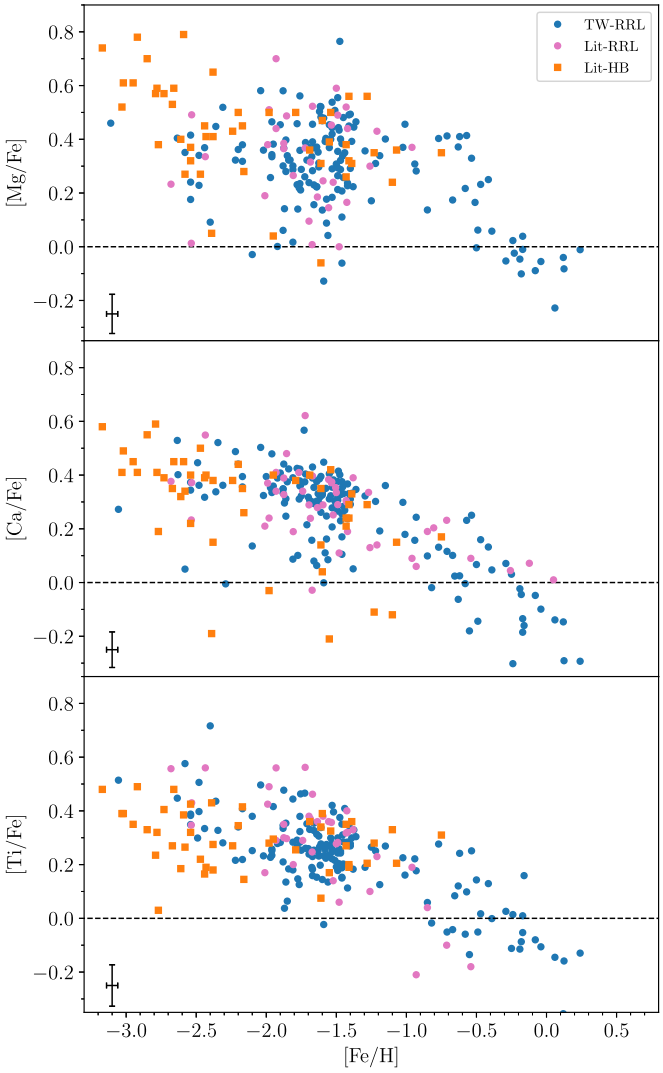

Figure 5. Abundances of Mg, Ca, and Ti for the TW-RRL (blue dots), Lit-RRL (pink dots), and Lit-HB (orange squares) samples. The error bars in the lower-left corner of each panel display typical uncertainties.

(ii) *Similar slopes for Mg, Ca, and Ti*—The investigated species display a well-defined slope when moving from the metal-poor to the metal-rich regime. The steady decrease in α enhancement is clearer in Ti and Ca for which the variation is of the order of $\sim$0.6 dex, but it is also present in Mg. Very metal-poor ([Fe/H] $\leqslant -2.2$) RRLs are strongly enhanced in α elements ([α/Fe] $\sim$ 0.4–0.5), while those approaching solar

iron abundance are depleted in α elements ($[\alpha/\mathrm{Fe}] \sim -0.2$ to -0.3; see also Prudil et al. 2020).

(iii) *Similar dispersion for Ca and Ti*—Both Ca and Ti display trends in tight agreement and can be considered the same within uncertainties. Their scatter remains of the order of 0.4 dex over the entire metallicity range and appears to be intrinsic because it is over three times larger than the typical errors (see typical error bars in the bottom-left corner of Figure 5).

The value of the plateau for these two species is not significantly different in our data. It bears mentioning that a disagreement between Ti and Ca in a given investigation may be a consequence of the adopted atomic lines and their transition parameters. Indeed, updated transition parameters derived from laboratory studies are only available for titanium. For calcium, a variety of parameters can be found, ranging from laboratory studies dating back to half a century ago to astrophysical determinations that use the Sun or nearby bright stars as a reference. Differences in the adopted lines and their oscillator strengths can result in abundances with variations of the order of 0.2 dex (Pancino et al. 2010). This limitation coupled with smaller sample sizes may have created difficulties in detecting the α-element depletion we observe in metal-rich RRLs (e.g., Liu et al. 2013).

(iv) *Larger dispersion for Mg*—Mg shows a large dispersion at metallicities lower than $[\mathrm{Fe/H}] \lesssim -1.2$. Measurement difficulties play a role in the scatter. The number of Mg lines is very limited, with mostly strong lines that easily saturate and must be discarded. This means that for several stars the Mg abundance is computed using only one or two transitions. Meanwhile, our spectra typically contained 5 to 15 lines of varied strengths for Ca and for Ti. As with calcium, magnesium lacks updated transition parameters from laboratory studies. An intrinsic spread, independent of the number of lines and their quality, but rather due to the mechanisms of Mg nucleosynthesis, may be present, and it is discussed in Section 5.4.

5.2. Comparison with Different Galactic Components

The range in metallicity covered by field RRLs is significantly larger than any other similar data sets in the literature. This is strikingly clear in a comparison with typical stars of different Galactic components, as shown in Figure 6. The RRLs cover the metal-poor ($[\mathrm{Fe/H}] \leqslant -2.5$) region of the halo and bulge, but they also extended to super-solar metallicities like the dwarfs and giants in the thin and thick disks.

As suggested by Nissen & Schuster (2010) and more recently by the near-infrared APOGEE survey by Hayes et al. (2018), there is evidence of a bimodal distribution in the [Mg/Fe] versus [Fe/H] plane for metallicities between -1.50 and -0.50 dex. This bimodality is not observed in our data, suggesting that it may an age-related phenomenon. In this same Mg versus iron plane, field RRLs, field stars, and GCs attain quite similar values in the halo, with a dispersion that allows only modest claims about a slope. On the other hand, field RRLs display a well-defined slope in Ca and in Ti when moving from $[\mathrm{Fe/H}] \approx -3.2$ to -1.3, while field stars and GCs display an almost constant value at $\approx$0.3 dex.

5.3. Comparison with Nearby Dwarf Galaxies

The current cold dark matter cosmological simulations suggest that the halo formed from the aggregation of protogalactic fragments—small galaxies form first and then merge to form larger galaxies (Dekel & Silk 1986; Bullock & Johnston 2005; Monachesi et al. 2019). The discovery of stellar streams and the merging of a massive dwarf galaxy like Sagittarius (Ibata et al. 1994), Gaia Enceladus (Helmi et al. 2018), and Sequoia (Myeong et al. 2019) provided further support to this hierarchical mechanism. Metallicity distribution functions can provide solid quantitative constraints on the mass assembly of the Galactic halo (Fiorentino et al. 2017); therefore, we also compared the current α-element abundances with similar abundances for RGs in nearby dwarf galaxies.

The data plotted in Figure 7 display the same comparison in Figure 6, but for α-element abundances of individual RG stars in both classical dwarf galaxies and ultrafaint dwarfs (UFDs). Note that in this comparison we are only taking into account measurements based on HR spectra.

The samples for Sagittarius and Fornax are marked by red stars and goldenrod diamonds, respectively. The comparison indicates a remarkable agreement in the metal-rich tail ($[\mathrm{Fe/H}] \geqslant -1.2$) between halo RRLs and RGs in Sagittarius and, in particular, the α-poor RRLs approaching solar iron abundance. The trend in the three different α-elements is similar across a range in iron abundance of over 1 dex, with marginal variations. In the case of the RGs in Fornax, however, the agreement with the RRL+HB sample is only present for metallicities between -1.3 and -1.8 dex. Indeed, the bulk of Fornax RGs are on overage more α poor than our sample.

Good agreement can also be seen in the metal-poor regime ($[\mathrm{Fe/H}] \leqslant -2.2$) between the RRL+HB sample and RGs in UFDs (gray crosses, data from Vargas et al. 2013). This is quite interesting because the age distribution in UFDs is narrower when compared to classical dSph galaxies. However, recent spectroscopic measurements are suggesting that the chemical abundance distributions of RGs in UFDs are inhomogeneous (Koch et al. 2008b; Weisz et al. 2014). The empirical framework becomes even more complex for the more massive dwarf galaxies because they exhibit a broad range of star formation histories and chemical enrichment histories (Tolstoy et al. 2009). Indeed, the α-element abundances for classical dwarf galaxies (light blue squares) have a dispersion in α abundances, at fixed iron content, that is significantly larger than the dispersion found in our sample. Note that this trend is also caused by the fact that the current α-element abundances are restricted, due to an observational bias, to bright RGs in nearby dwarf galaxies. This means that they typically cover a broad range in age. Fabrizio et al. (2015) has recently addressed this issue and found that old and intermediate-age stellar populations in the Carina dSph galaxy display a difference of $\sim$0.6 dex in α-element abundances (see also Koch et al. 2008a). Unfortunately, we still lack accurate abundance estimates of α elements in truly old stellar tracers (RRL and nonvariable HB stars) belonging to nearby dwarf galaxies to be compared to our sample.

5.4. Preliminary Circumstantial Evidence Concerning RRL Chemical Enrichment

As mentioned in Section 5.1, the plateau in the [X/Fe] versus [Fe/H] plane depends on the quality of the adopted

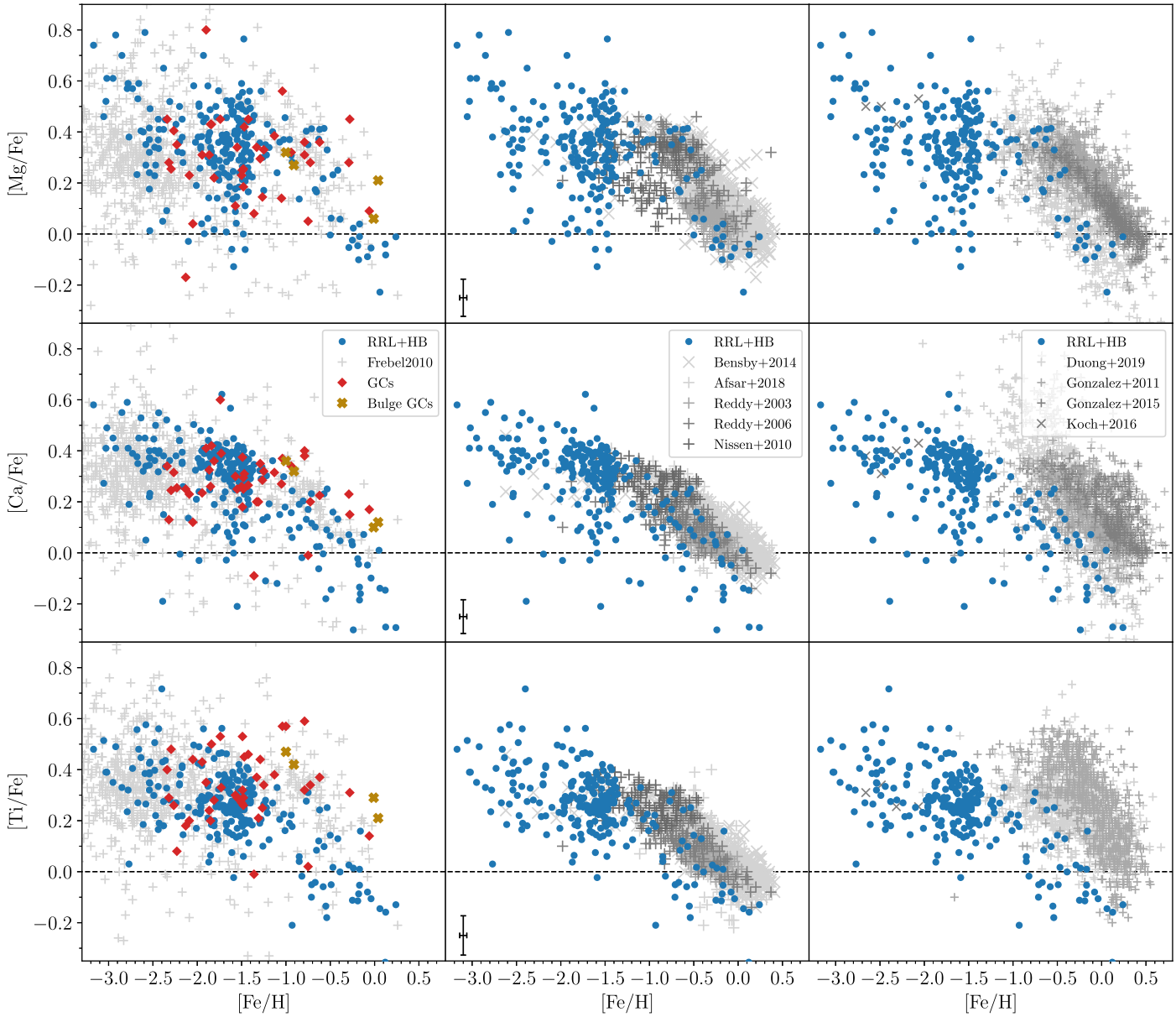

Figure 6. Abundances of Mg, Ca, and Ti for the RRL+HB sample, compared to three typical Galactic populations. Left: globular clusters and halo field stars. Middle: thin- and thick-disk field stars. Right: bulge field stars. References—GCs: Pritzl et al. (2005) and Carretta et al. (2009a, 2009b, 2010a); bulge GCs: Gonzalez et al. (2011). The remaining references are labeled according to the first author and year of publication: Frebel (2010), Bensby et al. (2014), Reddy et al. (2003, 2006), Afsar et al. (2018), Nissen & Schuster (2010), Duong et al. (2019), Gonzalez et al. (2011, 2015), and Koch et al. (2016).

atomic transition parameters. This is the reason why we are mainly interested in the trends among the different α elements. Yet, our results show very good agreement among Mg, Ca, and Ti, including the value of the plateau, in accordance with the data from Frebel (2010) shown in the rightmost panels of Figure 6. The same agreement is found with the very metal-poor halo dwarfs and giants investigated by Cayrel et al. (2004). The logarithmic fits of the [X/Fe] versus [Fe/H] planes agree within errors for the three species, and indeed, they are nearly identical for Ca and Ti across the whole metallicity range (Figure 8, bottom panel).

Magnesium displays a larger spread than Ca and Ti for both the RRL and the Lit-HB samples, and for the typical populations of each Galactic component (Figure 6). An intrinsic spread in Mg and deviations from the trends set by Ca and Ti may be present due to the dependence on progenitor mass and metallicity of the Mg yields. In theoretical models, the yields of Ca and Ti remain similar for a wide range of progenitor masses, but the same cannot be said for Mg. The production of the latter significantly increases in progenitors with large stellar masses (35 $M_{\odot}$; see Figure 6 of McWilliam 1997). Moreover, the production of Mg, at fixed stellar mass, depends on the metallicity. Indeed, it shows a marked decrease when moving from metal-poor/metal-intermediate to metal-rich progenitors (see Figures 2 and 4 in Kobayashi et al. 2006).

However, the current data indicate that [Mg/H], [Ca/H], and [Ti/H] vary in lockstep with one another, with negligible differences in their dispersion. Taken at face value, this result points to an early chemical enrichment that appears to be quite homogeneous for these three species over a wide range in iron abundance.

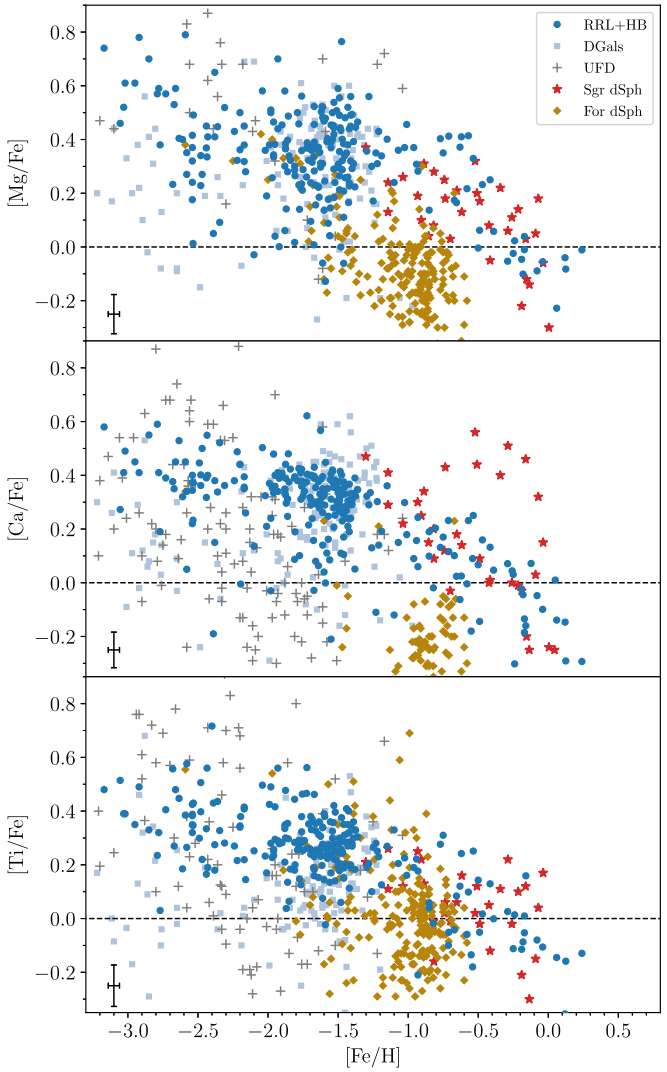

Figure 7. Abundances of Mg, Ca, and Ti for the RRL+HB sample, compared to stars in nearby dwarf galaxies. Red stars: Sagittarius dSph. Goldenrod diamonds: Fornax dSph. Light blue squares: Carina, Draco, Leo I, Sculptor, Sextans, and Ursa Minor. Gray crosses: ultrafaint dwarf galaxies. References—Shetrone et al. (2001), Tolstoy et al. (2003), Geisler et al. (2005), Sbordone et al. (2007), Aoki et al. (2009), Cohen & Huang (2009), Frebel et al. (2010), Carretta et al. (2010b), Letarte et al. (2010), Tafelmeyer et al. (2010), Starkenburg et al. (2013), Vargas et al. (2013), and Hendricks et al. (2014b).

The average [α/Fe] versus iron plane is quite homogeneous and properly fit by the logarithmic function

$$[\alpha/\mathrm{Fe}] = a + b\,\log(c - [\mathrm{Fe/H}]), \quad (1)$$

with parameters a, b, and c, and rms error as listed in Table 7. The fit is shown in both panels of Figure 8. We found no trends in the residuals of this fit against the pulsational properties, i.e., period and amplitude, of the RRL sample, nor any peculiar behavior when separating RRab and RRc stars. Furthermore, we did not observe a significant change in either the logarithmic fit parameters nor the residuals when removing Mg. As mentioned in Section 5.1, our spectra only have a small number of Mg lines, and so the weighted average of the three species favors Ca and Ti with their nearly identical trends. As the α elements considered in this work have different formation channels, we included the parameters for the same logarithmic function considering each individual chemical species

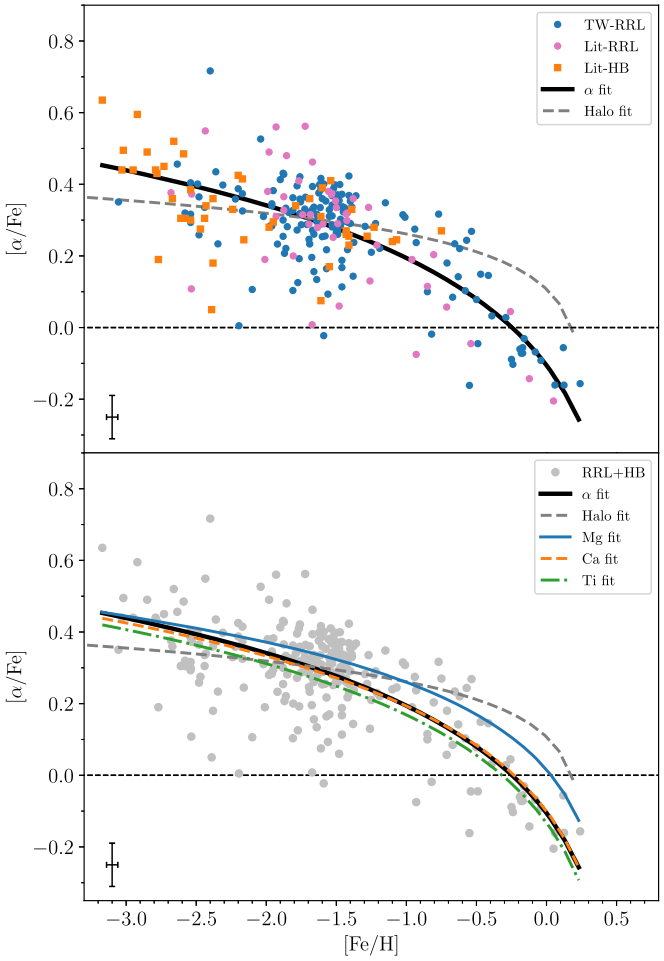

Figure 8. Top: average [α/Fe] abundances using Mg, Ca, and Ti, for the stars in the TW-RRL (blue dots), Lit-RRL (pink dots), and Lit-HB (orange squares) samples. See text for details on the averaging method. The full black line shows the logarithmic fit for the RRL and Lit-HB samples, and the dashed gray line shows the logarithmic fit for the halo field stars and GCs included in the left panels of Figure 6. Bottom: same as the top, but with the full RRL+HB sample shown as gray dots. The logarithmic fits for the individual species are shown for Mg (blue solid line), Ca (orange dashed line), and Ti (green dotted–dashed line).

Table 7
Parameters of the Logarithmic Fits (Equation (1))

Fit	a	b	c	rms
α	0.057 ± 0.064	0.690 ± 0.108	0.581 ± 0.190	0.10
Mg	0.175 ± 0.074	0.498 ± 0.139	0.479 ± 0.278	0.16
Ca	0.075 ± 0.070	0.639 ± 0.125	0.532 ± 0.216	0.12
Ti	0.047 ± 0.070	0.657 ± 0.124	0.534 ± 0.211	0.11
Halo	0.237 ± 0.013	0.229 ± 0.032	0.270 ± 0.021	0.19

Note. The parameters for the α, Mg, Ca, and Ti fits were derived using the full RRL+HB sample. The halo fit was derived considering all objects in the left panels of Figure 6 with the exception of the RRL+HB sample.

individually in Table 7. The corresponding fits are shown in the bottom panel of Figure 8.

The spread in α abundance steadily decreases when moving from the metal-poor/metal-intermediate into the more metal-rich ([Fe/H] $\geqslant -1.0$) regime. The Lit-HB sample does not reach higher metallicities, but this change in spread appears even when considering only the RRLs. Indeed, the spread in α-

element abundance decreases from ∼0.5 dex to ∼0.2 dex. The position of this sharp decrease in α abundance, the so-called "knee," is traditionally interpreted as evidence of the growing impact of SNe Ia. While the SNe II, with their short timescales, quickly enrich the interstellar medium with mainly α elements and some iron, the SNe Ia, with much longer timescales, begin to enrich the interstellar medium when it is already at higher metallicities, injecting it with mostly iron and causing a quick decrease of the α-to-iron ratio.

The RRL and HB stars appear to be, at fixed iron abundance, more α enhanced than typical halo objects (left panel of Figure 6) in the metal-poor ([Fe/H] $\leqslant = -2.0$) regime and more α poor than typical halo objects in the metal-rich ([Fe/H] $\geqslant -1.0$) regime. Indeed, a fit with the same logarithmic form shown above but applied to these typical halo objects is indicated by a dashed gray line in both panels of Figure 8. The corresponding parameters are listed in Table 7. This plain evidence could imply that the role played by SNe II in the halo chemical enrichment was more crucial in the metal-poor than in the metal-intermediate/metal-rich regime.

There is mounting evidence for a sizable sample of metal-rich HB stars that are also α poor (see Figure 12 in Afsar et al. 2018). Indeed, for iron abundances larger than ≈ -0.2 dex, their α-element abundance is either solar or lower. This finding, together with our results based on RRLs, indicates that the chemical enrichment in a significant fraction of metal-rich old field stars was mainly driven by SNe Ia with a minor contribution from SNe II. The lockstep variations we observed for [X/H] for the three species, and in particular the spread in Mg that is comparable to that of the other species (Section 5.1), point toward an early chemical enrichment driven by a homogeneous initial mass function over a wide range in iron abundance.

6. Summary and Future Perspectives

We performed the largest and most homogeneous measurement of α-element (Mg, Ca, Ti) and iron abundances for field RRLs (162) by using high-resolution spectroscopy. This data set was complemented with similar abundance estimates available in the literature for 46 field RRLs transformed into our metallicity scale by using objects in common. We ended up with a sample of old ($t \geqslant 10$ Gyr) stellar tracers (208 RRLs: 169 RRab, 38 RRc, 1 RRd) covering more than 3 dex in iron abundance ($-3.00 \leqslant$ [Fe/H] $\leqslant 0.24$). Note that the targets were selected to have Galactocentric distances ranging from ∼5 to ∼25 kpc. Therefore, they are solid beacons to investigate the early chemical enrichment of the Galactic halo.

We found that Mg, Ca, and Ti abundances vary, within the errors, in lockstep with one another and have similar scatter over the entire range in iron abundance. Furthermore, the trend in the [α/Fe] versus [Fe/H] plane displayed by field RRLs only partially follows the trend typical of other halo stellar populations. RRLs in the metal-poor regime, appear to be systematically more α-enhanced by ∼0.1 dex, while in the metal-rich regime, they are more α poor by ∼0.3 dex, i.e., a factor of 3 larger than the typical uncertainties. This is the first time this depletion in α elements is detected on the basis of a large, homogeneous, and coeval sample of old stellar tracers.

A comparison with nearby classical dwarf galaxies and UFD galaxies reveals a remarkable agreement between the halo RRLs and RGs in the Sagittarius dSph galaxy in the metal-rich regime. In the metal-poor regime, beyond the range of the Sagittarius dSph sample, the RRLs display better agreement with UFD galaxies than with more massive dwarf galaxies.

To further constrain the role played by stellar age in the early chemical enrichment of the halo, we took also into account similar elemental abundances for 46 field blue and red HB stars provided by For & Sneden (2010). These stars are either slightly hotter (blue) or slightly cooler (red) than RRLs; however, they share the same evolutionary phase (central helium burning) and the same old ($t \geqslant 10$ Gyr), low-mass progenitors. Theory and observations indicate that they only differ in their envelope mass. We found that RRLs and HB stars show the same trends in the [α/Fe] versus [Fe/H] planes. These findings support the halo early chemical enrichment, here traced by unambiguously old stellar tracers.

To overcome the possible occurrence of significant continuum placement uncertainty or saturated lines, we carefully selected lines with equivalent widths between 15 and 150 mÅ. Moreover, we selected several lines that could be measured over a significant fraction of the range in iron covered by the current RRL sample in order to verify that no systematic differences between different lines and chemical species influenced the trend in the [α/Fe] versus [Fe/H] plane. Finally, we also performed a comparison with spectroscopic standards (Arcturus) and with field metal-rich red HB stars (Afsar et al. 2018). We found that our iron and α-element abundances are, within the errors, in remarkable agreement with similar estimates available in the literature.

Chemical evolution models, for the chemical species discussed in this investigation, point to different dependencies of the yields on the stellar mass and the metallicity regime. This means that the current findings can be soundly adopted to constrain the chemical enrichment history of the halo. In passing, we also note that RRLs and HB stars cover a very narrow range in stellar masses; therefore, the comparison with similar Halo stellar tracers can provide useful insights into the role played by the initial mass function and the star formation rate during the halo's early formation.

Our findings concerning the impact that stellar age has on the analysis of the different [α/Fe] versus [Fe/H] planes is very promising. New spectroscopic surveys (WEAVE, Dalton 2016; 4MOST, de Jong et al. 2019; GALAH, De Silva et al. 2015; H3, Conroy et al. 2019; SDSSV, Kollmeier et al. 2017) based on high-resolution optical spectra will provide in a few years detailed halo elemental abundances not only for blue HB and red HB stars, but also for RRLs. This means the unique opportunity to investigate the fine structure in time and in Galactocentric distance of the halo's early chemical enrichment. A similar quantitative jump is also planned for the chemical enrichment of the Galactic bulge. Thanks to current (APOGEE, Majewski et al. 2017; WINERED, Ikeda et al. 2016) and near-future (CRIRES+ at VLT, Follert et al. 2014; MOONS at VLT, Cirasuolo et al. 2014; ERIS at VLT, Davies et al. 2018; PFS at Subaru, Tamura et al. 2018) spectroscopic surveys, detailed elemental abundances will also become available. This means the opportunity to constrain on a quantitative basis the chemical enrichment and the timescale of the Galactic spheroid, i.e., both the halo and the bulge.

The current spectroscopic measurements are a fundamental stepping stone for a detailed comparison between chemical evolution models and observations. Indeed, our RRL sample was built to provide a clean (concerning the age distribution) and homogeneous (concerning the methodological approach

and the spectroscopic data set) observational framework to compare with theoretical predictions (Cescutti 2008; Spitoni & Matteucci 2011; Limongi & Chieffi 2018).

We thank the anonymous referee for positive words regarding the content and cut of the paper and for pertinent suggestions that helped improve its readability. It is a pleasure to thank F. Matteucci and M. Palla for several detailed discussions concerning the role of α elements in constraining chemical evolution models, and E. Carretta for insightful discussions concerning the α elements in field and cluster stars.

This research has made use of the National Aeronautics and Space Administration (NASA) Astrophysics Data System, the National Institute of Standards and Technology (NIST) Atomic Spectra Database, the JVO Portal[31] operated by ADC/NAOJ, and the ESO Science Archive Facility.

Based on observations made with the Italian Telescopio Nazionale Galileo (TNG) operated on the island of La Palma by the Fundación Galileo Galilei of the INAF (Istituto Nazionale di Astrofisica) at the Spanish Observatorio del Roque de los Muchachos of the Instituto de Astrofisica de Canarias.

Some of the observations reported in this paper were obtained with the Southern African Large Telescope (SALT).

Based on observations collected at the European Organisation for Astronomical Research in the Southern Hemisphere under ESO programmes 0100.D-0339, 0101.D-0697, 0102.D-0281, 076.B-0055, 077.B-0359, 077.D-0633, 079.A-9015, 079.D-0262, 079.D-0462, 079.D-0567, 082.C-0617, 083.B-0281, 083.C-0244, 094.B-0409, 095.B-0744, 097.A-9032, 098.D-0230, 189.B-0925, 267.C-5719, 297.D-5047, 67.D-0321, 67.D-0554, 69.C-0423, 71.C-0097, 0100.D-0273, 083.C-0244, and 098.D-0230.

Funding for the SDSS and SDSS-II has been provided by the Alfred P. Sloan Foundation, the Participating Institutions, the National Science Foundation, the US Department of Energy, the National Aeronautics and Space Administration, the Japanese Monbukagakusho, the Max Planck Society, and the Higher Education Funding Council for England. The SDSS Web Site is http://www.sdss.org/. The SDSS is managed by the Astrophysical Research Consortium for the Participating Institutions. The Participating Institutions are the American Museum of Natural History, Astrophysical Institute Potsdam, University of Basel, University of Cambridge, Case Western Reserve University, University of Chicago, Drexel University, Fermilab, the Institute for Advanced Study, the Japan Participation Group, Johns Hopkins University, the Joint Institute for Nuclear Astrophysics, the Kavli Institute for Particle Astrophysics and Cosmology, the Korean Scientist Group, the Chinese Academy of Sciences (LAMOST), Los Alamos National Laboratory, the Max-Planck-Institute for Astronomy (MPIA), the Max-Planck-Institute for Astrophysics (MPA), New Mexico State University, Ohio State University, University of Pittsburgh, University of Portsmouth, Princeton University, the United States Naval Observatory, and the University of Washington.

We acknowledge financial support from US NSF under grants AST-1714534 (M.M., J.P.M.) and AST1616040 (C.S.). E.K.G., B.L., A.J.K.H., Z.P., and H.L. were supported by the Deutsche Forschungsgemeinschaft (DFG; German Research Foundation)—Project-ID 138713538—SFB 881 ("The Milky Way System," subprojects A03, A05, A11). E.V. acknowledges the Excellence Cluster ORIGINS Funded by the Deutsche Forschungsgemeinschaft (DFG; German Research Foundation) under Germany's Excellence Strategy-EXC-2094-390783311.

[31] http://jvo.nao.ac.jp/portal/

Appendix A
Comparison of Equivalent Widths

As a simple sanity check, we compared the equivalent widths (EWs) among pairs of stars with similar effective temperatures and with either similar iron or α abundance (Figure 9). The number of such pairs is limited due to the need not only for similar $T_{\rm eff}$ but also for a significant number of lines in common. The comparison is particularly difficult for stars with lower metallicities or at higher effective temperatures, as they have fewer lines and higher uncertainties overall.

The effective temperature is the parameter that most strongly affects the abundance of each individual line. Thus, a comparison further supports the real variations of [Fe/H] and [α/H] among our stars. For a difference of up to approximately 0.15 dex, the EWs for both stars visually coincide. This can be seen in the second row of the left column of Figure 9. For the other panels, the pair of stars have a difference in either [Fe/H] or [α/H] that can be visually detected by the fact that the EWs for the abundance that is similar show an identity relation, while the EWs for the abundance that is different are shifted from the identity to either higher or lower values.

Appendix B
NLTE Corrections and the Trend of Individual Lines

The absorption lines of a given chemical species display EWs that depend on the abundance of the element in question, which is directly related to the overall metallicity [M/H] and, consequently, to the [Fe/H] as well. In other words, the EWs of a given element will be smaller at lower metallicities and increase with increasing metallicity. This is of particular importance when analyzing the [X/Fe] versus [Fe/H] trend because a given line may be too weak at low [Fe/H] or too strong at high [Fe/H] and therefore only measured in a limited range of [Fe/H] values. Using several lines of different strengths ensures that the whole metallicity range is covered, but the transition parameters of different lines are subject to uncertainties that may result in significant disagreements between them and create spurious trends if one line is only available at lower metallicities and the other line only at higher metallicities. Therefore, the presence of one single line that covers a wide metallicity range is extremely valuable in order to confirm that any trends are real and not due to such systematics.

A few of the lines adopted in this work cover the entire metallicity range of the current sample. For Mg, no line is present in all metallicity regimes, but the domains of different lines are superposed in such a way that it is possible to verify they are on the same scale. Moreover, the overall behavior of Mg is in agreement with that of Ca and Ti. This is shown in Figure 10.

Different lines in the same chemical species may be subjected to different levels of NLTE effects. We obtained the values of NLTE corrections using the MPIA NLTE

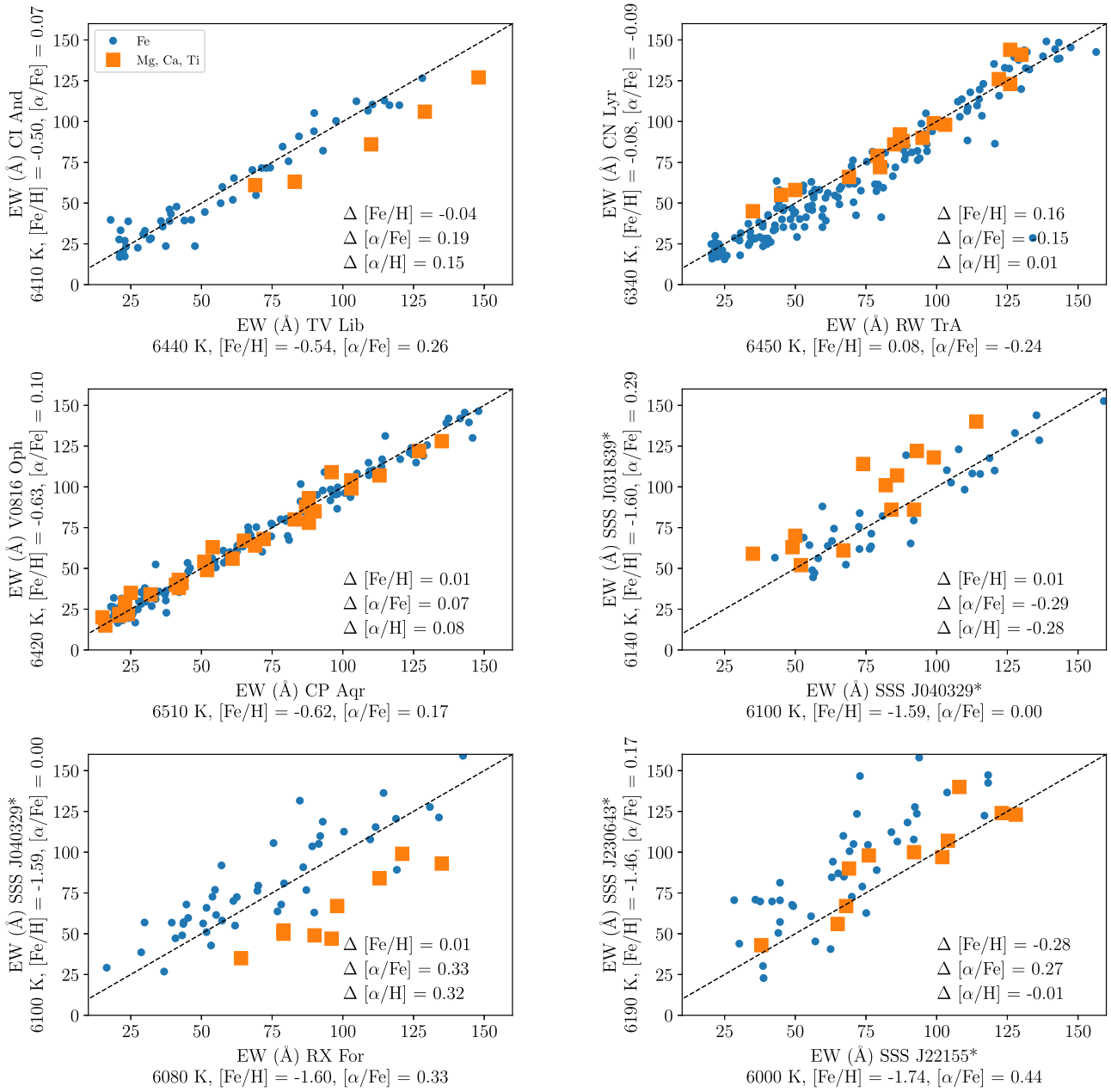

Figure 9. Comparison of equivalent widths for iron (blue dots) and α-element (orange squares) lines for stars at similar effective temperatures. The atmospheric parameters of interest for each star are shown in the axes. The difference between [Fe/H], [α/H], and [α/Fe] are shown in the left corner of each panel.

Spectrum Tools.[32] The corrections for the Mg (Bergemann et al. 2017), Ca (Mashonkina et al. 2007), and Ti (Bergemann 2011) lines were computed using 1D plane-parallel models for a set of typical RRL atmospheric parameters in the whole metallicity range covered by our sample. A few lines adopted in this work were not available for this analysis, namely the Mg lines at 8712.69 and 8717.83 Å; the Ca lines at 5581.97, 5601.29, 6471.66, 6493.78, 6499.65, and 6717.69 Å; the Ti I lines at 3729.81, 3741.06, 5036.46, and 5038.4 Å; and the Ti II lines at 4464.45, 6606.96, and 7214.73 Å. The results for the remaining lines are as follows.

(i) *Mg*: Most corrections for the seven available lines were under $\pm$0.05 dex, with the exception of the metal-poor tail, where four lines had corrections of the order of +0.14.

(ii) *Ca*: Most lines had corrections of the order of a staggering +0.4 dex. However, three lines (6166.4, 6449.8, and 6455.6 Å) display vanishing corrections, and yet, in our results, these lines are in good agreement with all others in any given star where they appear. We also note that choosing the spherical 1D models produced corrections as high as 1.0 dex. The source paper for the corrections does not quite cover the atmospheric parameters of RRL, but the closest values provide corrections of the order of 0.2 dex in the metal-poor regime for some of the lines, with smaller positive or negative corrections for the metal-rich regime. We have included the 6455.6 Å line as goldenrod stars in Figure 10. If the corrections were adopted, this line would remain largely unchanged, while the others were shifted +0.4 dex.

(iii) *Ti* I: All available lines displayed corrections of the order of +0.15 dex in the metal-rich regime, increasing to about

[32] Available at http://nlte.mpia.de/.

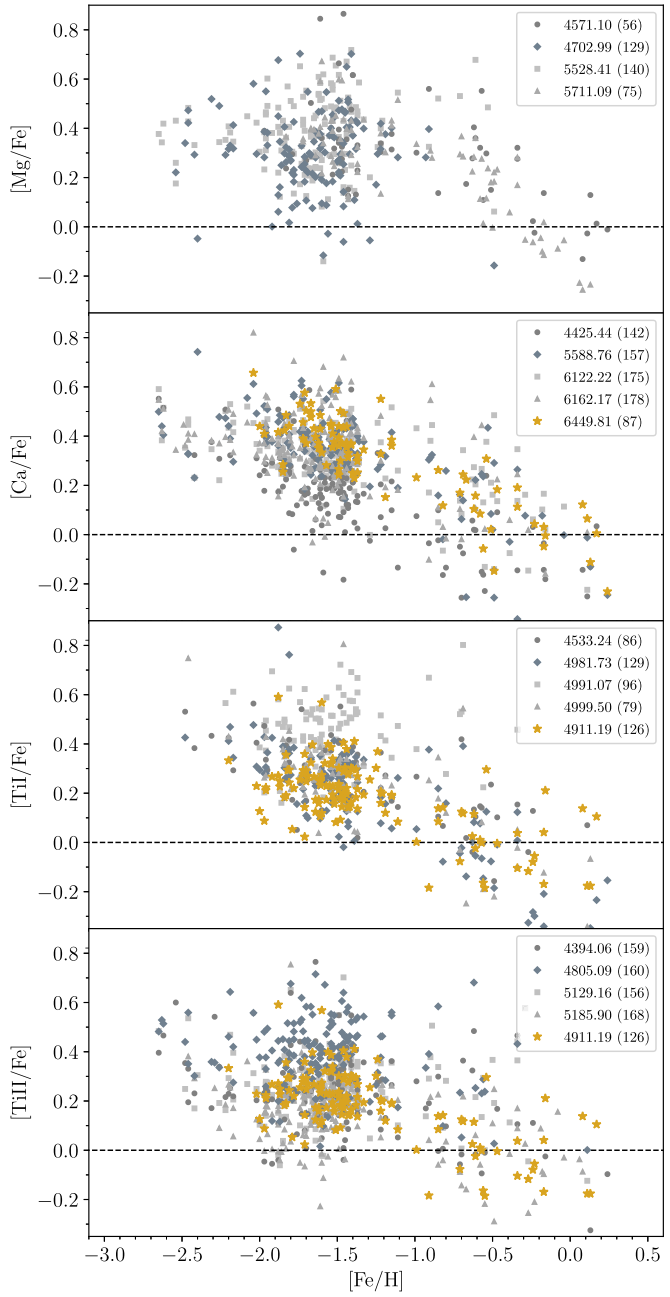

Figure 10. The [X/Fe] vs. [Fe/H] trend for individual lines for the three chemical species considered in this work. The lines shown as gray symbols are those with the greatest number of measurements. In red, we show two lines that do not require any NLTE correction. See text for details.

+0.30 dex in the metal-poor regime. This would further increase the slope in the [Ti I/Fe] versus [Fe/H] plane. Interestingly, the results for Ti I without any NLTE have a tighter scatter than those for Ti II with or without NLTE considerations.

(iv) *Ti* II: All available corrections were vanishing, except for a few lines where a shift of the order of +0.12 dex was present in the metal-poor regime. We note, however, that the corrections for the line at 4911.19 Å, shown as goldenrod stars in Figure 10, were zero.

Without considering the NLTE corrections, a few lines in our sample seem to be systematically higher than others (see, e.g., the Ti II lines at 4805.09 and 5185.90 Å in Figure 10); however, other lines follow either of the two sequences set by these lines or remain between them. As the trend in [X/Fe] versus [Fe/H] is the same for both sequences, taking the average value among all lines preserves it, and the higher σ of each α element accounts for this decision to include all available lines. The LTE analysis preserves both the internal consistency of our investigation and the possibility to readily compare it against other data sets in the literature.

ORCID iDs

J. Crestani https://orcid.org/0000-0001-8926-3496
V. F. Braga https://orcid.org/0000-0001-7511-2830
M. Fabrizio https://orcid.org/0000-0001-5829-111X
G. Bono https://orcid.org/0000-0002-4896-8841
C. Sneden https://orcid.org/0000-0002-3456-5929
G. Fiorentino https://orcid.org/0000-0003-0376-6928
F. Thévenin https://orcid.org/0000-0002-5032-2476
B. Chaboyer https://orcid.org/0000-0003-3096-4161
M. Dall'Ora https://orcid.org/0000-0001-8209-0449
E. K. Grebel https://orcid.org/0000-0002-1891-3794
M. Marengo https://orcid.org/0000-0001-9910-9230
C. Martínez-Vázquez https://orcid.org/0000-0002-9144-7726
M. Monelli https://orcid.org/0000-0001-5292-6380
J. P. Mullen https://orcid.org/0000-0002-1650-2764
P. B. Stetson https://orcid.org/0000-0001-6074-6830
J. Storm https://orcid.org/0000-0002-8627-6096
E. Valenti https://orcid.org/0000-0002-6092-7145

References

Afşar, M., Bozkurt, Z., Böcek Topcu, G., et al. 2018, AJ, 155, 240
Alonso, A., Arribas, S., & Martínez-Roger, C. 1999, A&AS, 140, 261
Alonso, A., Arribas, S., & Martínez-Roger, C. 2001, A&A, 376, 1039
Aoki, W., Arimoto, N., Sadakane, K., et al. 2009, A&A, 502, 569
Asplund, M., Grevesse, N., Sauval, A. J., & Scott, P. 2009, ARA&A, 47, 481
Barnes, Thomas G. I. I., Moffett, T. J., Hawley, S. L., Slovak, M. H., & Frueh, M. L. 1988, ApJS, 67, 403
Bensby, T., Feltzing, S., & Oey, M. S. 2014, A&A, 562, A71
Bergemann, M. 2011, MNRAS, 413, 2184
Bergemann, M., Collet, R., Amarsi, A. M., et al. 2017, ApJ, 847, 15
Bono, G. 2003, in RR Lyrae Distance Scale: Theory and Observations, ed. D. Alloin & W. Gieren, Vol. 635 (Berlin: Springer), 85
Bono, G., Braga, V. F., Crestani, J., et al. 2020, ApJL, 896, L15
Bullock, J. S., & Johnston, K. V. 2005, ApJ, 635, 931
Cacciari, C., Clementini, G., Castelli, F., & Melandri, F. 2000, in ASP Conf. Ser. 203, Revised Baade-Wesselink Analysis of RR Lyrae Stars, ed. L. Szabados & D. Kurtz (San Francisco, CA: ASP), 176
Cacciari, C., Clementini, G., & Fernley, J. A. 1992, ApJ, 396, 219
Carretta, E., Bragaglia, A., Gratton, R., et al. 2010a, ApJL, 712, L21
Carretta, E., Bragaglia, A., Gratton, R., & Lucatello, S. 2009a, A&A, 505, 139
Carretta, E., Bragaglia, A., Gratton, R. G., et al. 2009b, A&A, 505, 117
Carretta, E., Bragaglia, A., Gratton, R. G., et al. 2010b, A&A, 520, A95
Castelli, F., & Kurucz, R. L. 2003, in IAU Symp. 210, Modelling of Stellar Atmospheres, ed. N. Piskunov, W. W. Weiss, & D. F. Gray (San Francisco, CA: ASP), A20
Cayrel, R., Depagne, E., Spite, M., et al. 2004, A&A, 416, 1117
Cescutti, G. 2008, A&A, 481, 691
Chadid, M., Sneden, C., & Preston, G. W. 2017, ApJ, 835, 187
Cirasuolo, M., Afonso, J., Carollo, M., et al. 2014, Proc. SPIE, 9147, 91470N
Clementini, G., Cacciari, C., & Lindgren, H. 1990, A&AS, 85, 865
Clementini, G., Carretta, E., Gratton, R., et al. 1995, AJ, 110, 2319
Cohen, J. G. 1981, ApJ, 247, 869
Cohen, J. G., & Huang, W. 2009, ApJ, 701, 1053
Conroy, C., Naidu, R. P., Zaritsky, D., et al. 2019, ApJ, 887, 237
Cosentino, R., Lovis, C., Pepe, F., et al. 2012, Proc. SPIE, 8446, 84461V
Crause, L. A., Sharples, R. M., Bramall, D. G., et al. 2014, Proc. SPIE, 9147, 91476T
Crestani, J., Fabrizio, M., Braga, V. F., et al. 2021, ApJ, 908, 20

Curtis, S., Ebinger, K., Fröhlich, C., et al. 2019, ApJ, 870, 2
Dalton, G. 2016, in ASP Conf. Ser. 507, Multi-Object Spectroscopy in the Next Decade: Big Questions, Large Surveys, and Wide Fields, ed. I. Skillen, M. Balcells, & S. Trager (San Francisco, CA: ASP), 97
Davies, R., Esposito, S., Schmid, H. M., et al. 2018, Proc. SPIE, 10702, 1070209
de Jong, R. S., Agertz, O., Berbel, A. A., et al. 2019, Msngr, 175, 3
De Silva, G. M., Freeman, K. C., Bland-Hawthorn, J., et al. 2015, MNRAS, 449, 2604
Dekel, A., & Silk, J. 1986, ApJ, 303, 39
Dekker, H., D'Odorico, S., Kaufer, A., Delabre, B., & Kotzlowski, H. 2000, Proc. SPIE, 4008, 534
Duong, L., Asplund, M., Nataf, D. M., et al. 2019, MNRAS, 486, 3586
Fabrizio, M., Bono, G., Braga, V. F., et al. 2019, ApJ, 882, 169
Fabrizio, M., Nonino, M., Bono, G., et al. 2015, A&A, 580, A18
Fernley, J., & Barnes, T. G. 1996, A&A, 312, 957
Fernley, J. A., Skillen, I., Jameson, R. F., et al. 1990, MNRAS, 247, 287
Fiorentino, G., Bono, G., Monelli, M., et al. 2015, ApJL, 798, L12
Fiorentino, G., Monelli, M., Stetson, P. B., et al. 2017, A&A, 599, A125
Follert, R., Dorn, R. J., Oliva, E., et al. 2014, Proc. SPIE, 9147, 914719
For, B.-Q., & Sneden, C. 2010, AJ, 140, 1694
For, B.-Q., Sneden, C., & Preston, G. W. 2011, ApJS, 197, 29
Frebel, A. 2010, AN, 331, 474
Frebel, A., Simon, J. D., Geha, M., & Willman, B. 2010, ApJ, 708, 560
Geisler, D., Smith, V. V., Wallerstein, G., Gonzalez, G., & Charbonnel, C. 2005, AJ, 129, 1428
Gonzalez, O. A., Rejkuba, M., Zoccali, M., et al. 2011, A&A, 530, A54
Gonzalez, O. A., Zoccali, M., Vasquez, S., et al. 2015, A&A, 584, A46
Govea, J., Gomez, T., Preston, G. W., & Sneden, C. 2014, ApJ, 782, 59
Gratton, R., Sneden, C., & Carretta, E. 2004, ARA&A, 42, 385
Hajdu, G., Catelan, M., Jurcsik, J., et al. 2015, MNRAS, 449, L113
Harris, W. E. 1996, AJ, 112, 1487
Harris, W. E. 2010, arXiv:1012.3224
Hayes, C. R., Majewski, S. R., Shetrone, M., et al. 2018, ApJ, 852, 49
Helmi, A., Babusiaux, C., Koppelman, H. H., et al. 2018, Natur, 563, 85
Hendricks, B., Koch, A., Lanfranchi, G. A., et al. 2014a, ApJ, 785, 102
Hendricks, B., Koch, A., Walker, M., et al. 2014b, A&A, 572, A82
Ibata, R. A., Gilmore, G., & Irwin, M. J. 1994, Natur, 370, 194
Ikeda, Y., Kobayashi, N., Kondo, S., et al. 2016, Proc. SPIE, 9908, 99085Z
Jones, R. V., Carney, B. W., & Latham, D. W. 1988, ApJ, 326, 312
Karczmarek, P., Wiktorowicz, G., Iłkiewicz, K., et al. 2017, MNRAS, 466, 2842
Kaufer, A., Stahl, O., Tubbesing, S., et al. 1999, Msngr, 95, 8
Kervella, P., Gallenne, A., Remage Evans, N., et al. 2019, A&A, 623, A116
Kobayashi, C., Umeda, H., Nomoto, K., Tominaga, N., & Ohkubo, T. 2006, ApJ, 653, 1145
Koch, A., Grebel, E. K., Gilmore, G. F., et al. 2008a, AJ, 135, 1580
Koch, A., McWilliam, A., Grebel, E. K., Zucker, D. B., & Belokurov, V. 2008b, ApJL, 688, L13
Koch, A., McWilliam, A., Preston, G. W., & Thompson, I. B. 2016, A&A, 587, A124
Kollmeier, J. A., Zasowski, G., Rix, H.-W., et al. 2017, arXiv:1711.03234
Lambert, D. L., Heath, J. E., Lemke, M., & Drake, J. 1996, ApJS, 103, 183
Lawler, J. E., Guzman, A., Wood, M. P., Sneden, C., & Cowan, J. J. 2013, ApJS, 205, 11
Lemasle, B., de Boer, T. J. L., Hill, V., et al. 2014, A&A, 572, A88
Letarte, B., Hill, V., Tolstoy, E., et al. 2010, A&A, 523, A17
Limongi, M., & Chieffi, A. 2018, ApJS, 237, 13
Liu, S., Zhao, G., Chen, Y.-Q., Takeda, Y., & Honda, S. 2013, RAA, 13, 1307
Liu, T., & Janes, K. A. 1989, ApJS, 69, 593
Majewski, S. R., Schiavon, R. P., Frinchaboy, P. M., et al. 2017, AJ, 154, 94
Mashonkina, L., Korn, A. J., & Przybilla, N. 2007, A&A, 461, 261
Matteucci, F., & Brocato, E. 1990, ApJ, 365, 539
Matteucci, F., & Greggio, L. 1986, A&A, 154, 279
Mayor, M., Pepe, F., Queloz, D., et al. 2003, Msngr, 114, 20
McWilliam, A. 1997, ARA&A, 35, 503
McWilliam, A. 2016, PASA, 33, e040
McWilliam, A., Wallerstein, G., & Mottini, M. 2013, ApJ, 778, 149
Monachesi, A., Gómez, F. A., Grand, R. J. J., et al. 2019, MNRAS, 485, 2589
Myeong, G. C., Vasiliev, E., Iorio, G., Evans, N. W., & Belokurov, V. 2019, MNRAS, 488, 1235
Nissen, P. E., & Schuster, W. J. 2010, A&A, 511, L10
Noguchi, K., Aoki, W., Kawanomoto, S., et al. 2002, PASJ, 54, 855
Pancino, E., Britavskiy, N., Romano, D., et al. 2015, MNRAS, 447, 2404
Pancino, E., Carrera, R., Rossetti, E., & Gallart, C. 2010, A&A, 511, A56
Pietrzyński, G., Thompson, I. B., Gieren, W., et al. 2012, Natur, 484, 75
Pilachowski, C. A., Sneden, C., & Wallerstein, G. 1983, ApJS, 52, 241
Pritzl, B. J., Venn, K. A., & Irwin, M. 2005, AJ, 130, 2140
Prudil, Z., Dékány, I., Grebel, E. K., & Kunder, A. 2020, MNRAS, 492, 3408
Prudil, Z., Skarka, M., Liška, J., Grebel, E. K., & Lee, C. U. 2019, MNRAS, 487, L1
Ramírez, I., & Allende Prieto, C. 2011, ApJ, 743, 135
Reddy, B. E., Lambert, D. L., & Allende Prieto, C. 2006, MNRAS, 367, 1329
Reddy, B. E., Tomkin, J., Lambert, D. L., & Allende Prieto, C. 2003, MNRAS, 340, 304
Reichert, M., Hansen, C. J., Hanke, M., et al. 2020, A&A, 641, A127
Salaris, M., & Weiss, A. 1998, A&A, 335, 943
Savino, A., Koch, A., Prudil, Z., Kunder, A., & Smolec, R. 2020, A&A, 641, A96
Sbordone, L., Bonifacio, P., Buonanno, R., et al. 2007, A&A, 465, 815
Shetrone, M. D., Côté, P., & Sargent, W. L. W. 2001, ApJ, 548, 592
Sneden, C. 1973, ApJ, 184, 839
Sneden, C., Lambert, D. L., & Whitaker, R. W. 1979, ApJ, 234, 964
Sneden, C., Preston, G. W., Chadid, M., & Adamów, M. 2017, ApJ, 848, 68
Spitoni, E., & Matteucci, F. 2011, A&A, 531, A72
Starkenburg, E., Hill, V., Tolstoy, E., et al. 2013, A&A, 549, A88
Tafelmeyer, M., Jablonka, P., Hill, V., et al. 2010, A&A, 524, A58
Tamura, N., Takato, N., Shimono, A., et al. 2018, Proc. SPIE, 10702, 107021C
Timmes, F. X., Woosley, S. E., & Weaver, T. A. 1995, ApJS, 98, 617
Tody, D. 1993, in ASP Conf. Ser. 52, Astronomical Data Analysis Software and Systems II, ed. R. J. Hanisch, R. J. V. Brissenden, & J. Barnes (San Francisco, CA: ASP), 173
Tolstoy, E., Hill, V., & Tosi, M. 2009, ARA&A, 47, 371
Tolstoy, E., Venn, K. A., Shetrone, M., et al. 2003, AJ, 125, 707
VandenBerg, D. A., Brogaard, K., Leaman, R., & Casagrande, L. 2013, ApJ, 775, 134
Vargas, L. C., Geha, M., Kirby, E. N., & Simon, J. D. 2013, ApJ, 767, 134
Venn, K. A., Irwin, M., Shetrone, M. D., et al. 2004, AJ, 128, 1177
Vernet, J., Dekker, H., D'Odorico, S., et al. 2011, A&A, 536, A105
Walker, A. R., Martínez-Vázquez, C. E., Monelli, M., et al. 2019, MNRAS, 490, 4121
Wallerstein, G., Gomez, T., & Huang, W. 2012, Ap&SS, 341, 89
Wallerstein, G., Greenstein, J. L., Parker, R., Helfer, H. L., & Aller, L. H. 1963, ApJ, 137, 280
Wallerstein, G., Iben, Icko J., Parker, P., et al. 1997, RvMP, 69, 995
Weber, M., Granzer, T., & Strassmeier, K. G. 2012, Prov. SPIE, 8451, 84510K
Weisz, D. R., Dolphin, A. E., Skillman, E. D., et al. 2014, ApJ, 789, 148
Wood, M. P., Lawler, J. E., Sneden, C., & Cowan, J. J. 2013, ApJS, 208, 27
Woosley, S. E., & Weaver, T. A. 1995, ApJS, 101, 181